

# HV-BEV: Decoupling Horizontal and Vertical Feature Sampling for Multi-View 3D Object Detection

Di Wu, Feng Yang, *Member, IEEE*, Benlian Xu, Pan Liao, Wenhui Zhao, Dingwen Zhang, *Member, IEEE*

**Abstract**—The application of vision-based multi-view environmental perception system has been increasingly recognized in autonomous driving technology, especially the BEV-based models. Current state-of-the-art solutions primarily encode image features from each camera view into the BEV space through explicit or implicit depth prediction. However, these methods often focus on improving the accuracy of projecting 2D features into corresponding depth regions, while overlooking the highly structured information of real-world objects and the varying height distributions of objects across different scenes. In this work, we propose HV-BEV, a novel approach that decouples feature sampling in the BEV grid queries paradigm into horizontal feature aggregation and vertical adaptive height-aware reference point sampling, aiming to improve both the aggregation of objects' complete information and generalization to diverse road environments. Specifically, we construct a learnable graph structure in the horizontal plane aligned with the ground for 3D reference points, reinforcing the association of the same instance across different BEV grids, especially when the instance spans multiple image views around the vehicle. Additionally, instead of relying on uniform sampling within a fixed height range, we introduce a height-aware module that incorporates historical information, enabling the reference points to adaptively focus on the varying heights at which objects appear in different scenes. Extensive experiments validate the effectiveness of our proposed method, demonstrating its superior performance over the baseline across the nuScenes dataset. Moreover, our best-performing model achieves a remarkable 50.5% mAP and 59.8% NDS on the nuScenes testing set.

**Index Terms**—3D Object Detection, Multi-View, Bird's-Eye View (BEV) Representation, Multi-Camera, Autonomous Driving.

## I. INTRODUCTION

3D object detection is a fundamental task in intelligent vehicle perception systems, focused on estimating the locations, sizes, and categories of key objects in traffic scenarios—such as vehicles, pedestrians, cyclists, and traffic cones—in the ego-vehicle coordinate system [1]. Although

This work was supported in part by the National Natural Science Foundation of China (No. 61374159), Shaanxi Natural Fund (No. 2018MJ6048), Space Science and Technology Fund, the Foundation of CETC Key Laboratory of Data Link Technology (CLDL-20182316, CLDL20182203), and the Suzhou municipal science and technology plan project (No. SYG202351). (Corresponding author: Feng Yang and Benlian Xu.)

D. Wu, Feng Yang, Pan Liao and Wenhui Zhao are with the school of automation, Northwestern Polytechnical University, Xi'an Shanxi 710072, China (e-mail: wu\_di821@mail.nwpu.edu.cn; yangfeng@nwpu.edu.cn; liaopan@mail.nwpu.edu.cn; zhw2024202513@mail.nwpu.edu.cn; zdw2006yyy@nwpu.edu.cn).

Benlian Xu is with the school of electronic and information engineering, Suzhou University of Science and Technology, Suzhou Jiangsu 215009, China (e-mail: xu\_benlian@usts.edu.cn).

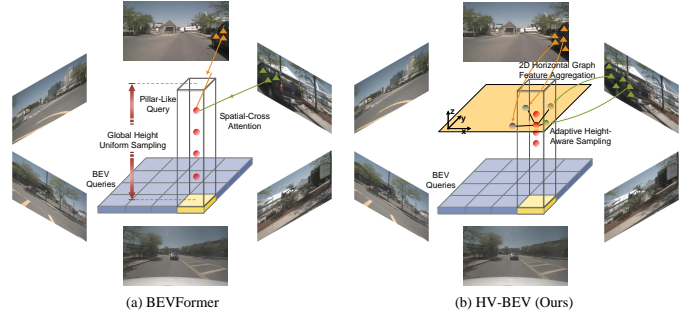


Fig. 1. The multi-view feature sampling comparison between (a) BEVFormer and (b) our HV-BEV. BEVFormer extracts local area features by uniformly sampling several reference points across the global height range within each pillar-like query and projecting them onto corresponding views. In contrast, our HV-BEV adopts adaptive height-aware sampling and constructs a graph for each reference point on the horizontal BEV plane, aggregating features from relevant regions to enhance feature coherence and improve network adaptability.

LiDAR provides direct distance measurements that facilitate 3D detection [2]–[6], its high cost and limited maintainability make cameras—cost-effective devices capable of capturing rich semantic information—an essential choice for deployment. By strategically positioning cameras at various angles around the vehicle, the system can achieve comprehensive perception of its surroundings. Consequently, multi-view visual 3D object detection remains one of the central focuses of ongoing research [7]–[9].

Recently, BEV-based 3D perception has gained widespread attention [10]–[12] due to the ability of BEV feature representation to model a complete, scale-consistent environment around the vehicle within a unified coordinate system, making it more suitable for downstream tasks such as path planning and control. BEV-based 3D object detection can be broadly categorized into two major methods: explicit and implicit depth estimation [8], based on how 2D features are transformed into 3D space. Explicit depth-based methods primarily utilize depth estimation networks to predict depth distribution in perspective views (PV), transforming PV feature maps into 3D space using determined camera parameters [13]–[16]. Instead of the intermediate depth estimation step, implicit methods rely on sophisticated view transformation networks to extract 3D information embedded in the 2D images without the need for a depth map [17]–[19], [21], [22].

Most of these existing methods focus on minimizing the feature localization errors caused by depth estimation inac-

curacies, while neglecting the 3D structural information of real-world objects. In other words, they pay little attention to the global representation of regions associated with an object when encoding BEV features, resulting in insufficient feature aggregation. While some works have addressed this issue with promising results [23]–[25], they are predominantly centered around sparse object query-based schemes, which are specifically designed for the single task of 3D object detection and are difficult to extend to other tasks, i.e., map segmentation, by simply replacing the task head or transform into multi-task models. In addition, most BEV-based methods either “splat” frustum features through Voxel/Pillar Pooling [13], [15], [27] or directly cross-encode image features into a flattened BEV grid plane [18], leading to the collapse of the height dimension and causing the model to overlook crucial height information. Different types of objects may exist at various heights [26], and we believe this height information should be fully utilized to assist the network in exploring the intrinsic properties of different objects. Moreover, the network should adaptively focus on the potential local heights of objects in different scenes, without dispersing its attention across all possible heights within the global height range. This is because, as we know, in real-world road scenarios, it is rare to encounter multiple objects occupying different heights at the same location simultaneously.

In this paper, we take BEVFormer [18], a representative work of the BEV grid query-based approach, as our baseline and propose a comprehensive 3D object detection framework named HV-BEV that decouples multi-view feature sampling in the horizontal BEV plane and vertical height direction. In the vanilla BEVFormer, multi-view feature sampling is achieved by projecting the 3D reference points located at the center of the corresponding cell region of each BEV query and uniformly sampled across the global height range to the hit views and applying deformable attention [20], as shown in Fig. 1(a). This sampling approach retrieves the corresponding image features for each BEV grid region from different views and implicitly modeling height information; However, it does not fully account for the structured features of 3D objects, particularly the cohesive nature of height information and the interdependencies across different dimensions. We identified that large or near-ego objects are sometimes missed or inaccurately estimated due to occupying multiple BEV grid regions or appearing in multiple camera views through observation. This phenomenon is primarily caused by insufficient feature aggregation in the horizontal dimension. To address this, we propose a horizontal cross-view feature aggregation module, which constructs a dynamic graph for each 3D reference point on the horizontal BEV plane to aggregate global features of the object from different grid regions and views, seen in Fig. 1(b). However, relying solely on horizontal feature aggregation is not enough, as different objects do not exist along a single horizontal line; rather, their heights vary with scene context and object class. Motivated by this, we introduce an adaptive height-aware sampling strategy as shown in Fig. 1(b). The height distributions from aligned historical BEV features and current BEV queries are fused and guide vertical height sampling of 3D reference points, allowing the network

to adaptively focus on the most relevant height for each object. The training of this module is done in a sparse way, using only 3D annotated bounding boxes without extra LiDAR points supervision. By decoupling feature sampling in different dimensions, the model can concentrate on information of value across various directions, yielding a more efficient global feature sampling strategy. Notably, while this paper evaluates the performance of HV-BEV using 3D object detection as the primary task for model training and prediction, our approach can be easily extended to other BEV-based perception tasks, such as map segmentation and lane detection.

Our contributions can be concluded as follows:

- We propose a multi-view 3D object detection method based on the BEV grid query paradigm, which decouples horizontal and vertical feature sampling to fully exploit 3D spatial information, achieving superior detection performance.
- We design a horizontal cross-view feature aggregation module that fuses relevant structured features of the object from different camera images and grid cell regions.
- We propose an adaptive height-aware sampling strategy in the vertical dimension to guide the network in identifying relevant object heights of interest. To achieve this, we introduce a deep supervision mechanism that operates without requiring additional LiDAR information.
- We conduct extensive experiments on the challenging public dataset nuScenes to validate the effectiveness of the proposed method. Our HV-BEV outperforms the baseline model across all evaluated metrics and exhibits outstanding performance within the camera-based 3D object detection community.

## II. RELATED WORK

### A. Explicit 3D Object Detection

The explicit-based methods utilize camera imaging principles to directly estimate the depth of each pixel in the image, enabling precise construction of 3D features. LSS [27] is a foundational work in this category, predicting the discrete depth distribution [28] of pixel points and, through a novel outer product with 2D image features, lifting these features into a frustum-like 3D perspective space to simulate feature point distribution along the line of sight. The BEVDet series [13], [14] follows the LSS paradigm, introducing a versatile framework for 3D object detection composed of four main modules: an image encoder, a view transformation module, a BEV encoder, and a task-specific head. BEVDepth [15] introduces lidar point cloud supervision for the depth estimation and encodes camera parameters into the network, enhancing robustness and accuracy in depth prediction and thereby improving detection performance. BEVStereo [16] enhances depth estimation by utilizing two-frame stereo images, predicting depth from both single-frame features and temporal stereo information. SOLOFusion [29] further enhances single-frame depth prediction by generating a cost volume from long-term historical images. FB-BEV [30] introduces a depth-aware back-projection process to refine the sparse BEV representation generated by the LSS-style forward projection. BEVNeXt

[31] argues that long-term fusion strategies, like those in SOLOFusion [29], [32], are constrained by limited receptive fields; thus, it expands the receptive field and enhances object-level BEV features derived through backward projection by incorporating CRF-modulated depth embeddings. Since these methods rely on depth prediction to accomplish the 2D-to-3D transformation, most approaches aim to enhance BEV representation by improving depth prediction accuracy through various strategies. However, depth estimation inevitably introduces errors that accumulate as network layers deepen.

### B. Implicit 3D Object Detection

Following the successful application of transformer [34]–[36] in computer vision [37]–[39], many query-based 3D detection frameworks have emerged, leveraging the transformer’s powerful feature encoding capabilities to eliminate the need for explicit depth prediction step. These frameworks can be categorized into sparse query-based methods, like DETR3D [17], which extract relevant features from 2D images using 3D queries, and dense query-based methods, like BEVFormer [18], [19], which predefine BEV grid queries to query corresponding BEV features from multi-view images. Considering the limitations of DETR3D’s single-point sampling in capturing global representations, the PETR series [21], [22] introduces a streamlined framework that bypasses direct 2D-to-3D transformation. Instead, it encodes 2D features with 3D positional embeddings, enabling the network to capture 3D spatial awareness. Graph-DETR3D [23] identifies ”truncated instances” at image boundary regions as a primary bottleneck limiting the detection performance of DETR3D [17]. To mitigate this issue, it introduces a dynamic 3D graph structure between each object queries and 2D feature maps, further extending this spatial graph into a 4D spatio-temporal space [24]. The Sparse4D series [25], [33] generates a set of keypoints for each instance’s anchor box, leveraging these keypoints to aggregate instance features across multiple time steps, scales, and viewpoints. While sparse query-based methods offer a balance between accuracy and speed, dense query-based approaches are better suited for multi-task extension due to their unified BEV representation. This paper aims to enhance the global spatial awareness of such models by using BEVFormer as the baseline.

### C. Height-Aware 3D Object Detection

Height information is often overlooked in BEV-based 3D object detection, yet it contains valuable object attribute features; for example, traffic cones are typically close to the ground, while buses are relatively tall. BEV-SAN [26] is the first to incorporate height-specific features of different objects within the network, using a height histogram of LiDAR points to define the upper and lower bounds of local BEV slices. This approach captures features across various heights in BEV space and fuses them with global BEV features, proving effective in increasing detection accuracy. HeightFormer [40] further demonstrates the equivalence of predicting height in BEV and predicting depth in images for 2D-to-3D mapping, presenting a BEV detection framework that explicitly models

height as an alternative to depth-based methods. BEVHeight [41], [42] focuses on improving 3D object detection performance for roadside applications, recognizing that depth-based methods, when directly transferred, often perform poorly with roadside cameras. This limitation arises because the depth of distant objects and the ground depth are nearly indistinguishable from a roadside camera’s perspective. To address this, BEVHeight leverages the more stable information provided by object height, enabling robust detection outcomes. OC-BEV [43] refines the reference point sampling in BEVFormer by introducing an object focused sampling mechanism. While it increases the sampling density in high-frequency height regions by presetting a local height range and does not fully exploit object height embeddings within the network. This paper explicitly extracts height information from BEV features to adaptively determine the heights of interest, facilitating a feature sampling method that is more generalizable and adaptable to diverse scenes.

## III. METHODS

### A. Revisiting to BEVFormer-Style Feature Sampling

To clearly present our proposed framework, we first review the feature sampling method in the baseline BEVFormer. It initially employs a backbone network to extract multi-view feature maps  $F_t = \{F_t^i\}_{i=1}^{N_{\text{view}}}$  from multi-view images, where  $F_t^i$  is the features of the  $i$ -th view at current timestamp  $t$ . It then introduces a BEV feature encoder structured similarly to a transformer decoder, consisting of multiple encoder layers in sequence. Each layer takes grid-shaped BEV queries  $Q \in \mathbb{R}^{H \times W \times C}$  as input, where  $H, W$  denotes the shape of BEV plane and  $C$  is the channel number, and progressively refines the current BEV features  $B_t$  through temporal self-attention with historical BEV features  $B_{t-1}$ , spatial cross-attention with the multi-view feature maps  $F_t$ , and additional transformer decoder components. Specifically, each query  $Q_p \in \mathbb{R}^{1 \times C}$  of  $Q$ , representing a rectangular region centered at  $p \in (x, y)$  in the BEV plane, first leverages temporal self-attention (TSA) to model temporal relationships from aligned historical BEV features  $B'_{t-1}$  to capture the sequential associations of objects over time:

$$\text{TSA}(Q_p, \{Q, B'_{t-1}\}) = \sum_{V \in \{Q, B'_{t-1}\}} \text{DefAttn}(Q_p, p, V), \quad (1)$$

where  $\text{DefAttn}(\cdot)$  is the deformable attention [20] and  $\{\cdot\}$  denotes the concatenation operation of two tensors. After applying a residual connection and a layer normalization (Add&Norm) [34] to the output BEV queries, spatial cross-attention (SCA) is then used to aggregate spatial information from multi-view features:

$$\text{SCA}(Q_p, F_t) = \frac{1}{|\mathcal{V}_{hit}|} \sum_{i \in \mathcal{V}_{hit}} \sum_{j=1}^{N_{\text{ref}}} \text{DefAttn}(Q_p, \mathcal{P}(p, i, j), F_t^i), \quad (2)$$

where  $N_{\text{ref}}$  denotes the number of 3D reference points uniformly sampled within a predetermined height range for each query  $Q_p$ , centered at the horizontal coordinate  $p(x, y)$  and

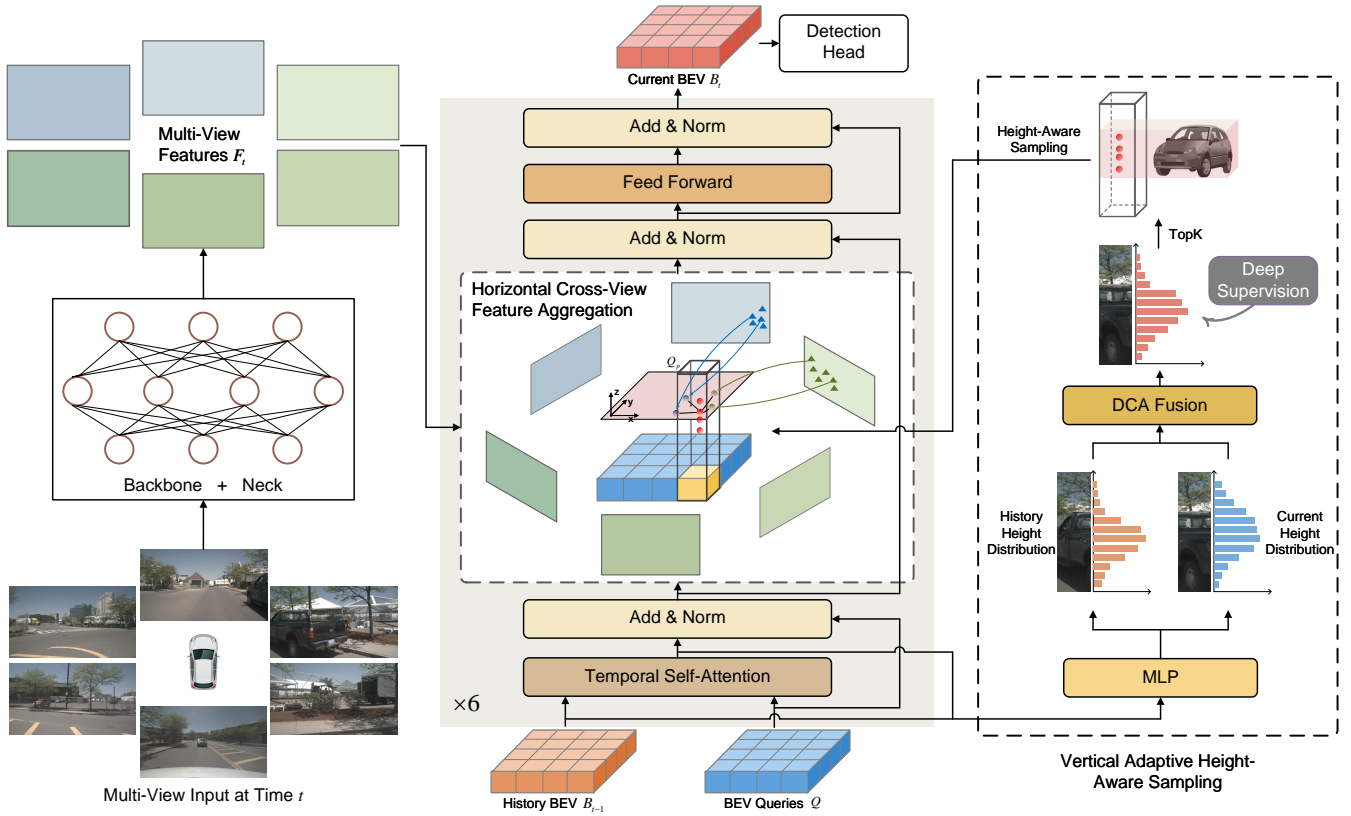


Fig. 2. Overall architecture of HV-BEV. Aligning with BEVFormer, we begin by using an image encoder to extract multi-view image features. Within the six-layer BEV encoder, we introduce two decoupled modules that respectively handle intrinsic height awareness and cross-view feature aggregation. The *Vertical Adaptive Height-Aware module* is designed to capture the potential height distribution of objects within each BEV grid, aiding in the sampling of 3D reference points. Leveraging these height-aware 3D reference points, the *Horizontal Cross-View Feature Aggregation module* constructs a graph structure on the BEV plane to explore spatial features from neighboring regions.

$\mathcal{V}_{hit}$  represents the hit views associated with the  $j$ -th reference point, obtained by projecting it via the function  $\mathcal{P}(p, i, j)$ . Following the temporal and spatial feature interactions via TSA and SCA, the resulting BEV queries are subjected to passed through an Add&Norm layer, then a forward propagation network (FFN) [34] and the last Add&Norm layer, yielding the final refined BEV features  $B_t$ .

### B. Overall Framework

As illustrated in Fig. 2, our HV-BEV follows the 6-layer encoder architecture of BEVFormer, with the primary difference being an improved multi-view feature sampling method within each layer. Specifically, we first employ an image encoder—comprising a backbone, such as ResNet [44], and a neck, like FPN [45]—to extract multi-view features  $F_t$  from the multi-view images at time  $t$ , which then serve as input for the horizontal cross-view feature aggregation module in the next BEV encoder.

A BEV encoder layer receives learnable BEV queries  $Q$  and the preserved BEV features  $B_{t-1}$  from the previous time step as input. We first apply a standard temporal self-attention layer to query temporal information from historical BEV as Eq.(1). Following this, a vertical height-aware sampling module (Sec. III-C) integrates the predicted height distribution from each  $Q_p$  of the current BEV queries, obtained through a shared MLP

layer, with the historical height distribution generated from  $B_{t-1}$  to sample  $N_{ref}$  discrete height values from the fused height distribution, setting these as the heights of the  $N_{ref}$  3D reference points for each query  $Q_p$ . Notably, by introducing deep supervision into this module, the BEV queries are guided to focus on the height ranges where objects are most likely to appear. In the horizontal cross-view feature aggregation module (Sec. III-D), each 3D reference point learns a dynamic graph within its height-specific BEV plane, projecting all the nodes in this graph onto multi-view images to fully aggregate spatial features from hit views. This approach allows for comprehensive integration of neighboring regions' spatial information that may appear in different views, further refining BEV features. After passing through additional standard layers (FFN, Add&Norm), the refined BEV features are fed as input queries to the successive BEV encoder layer and iteratively enhanced, producing the final BEV features, which are then utilized by task-specific heads for 3D detection and other perception tasks.

### C. Vertical Adaptive Height-Aware Sampling

In HeightFormer, the authors use attention weights to compute a weighted average of predefined anchor heights within a BEV sample, thereby visualizing how common SCA implicitly encodes height information. Instead of sampling at fixed

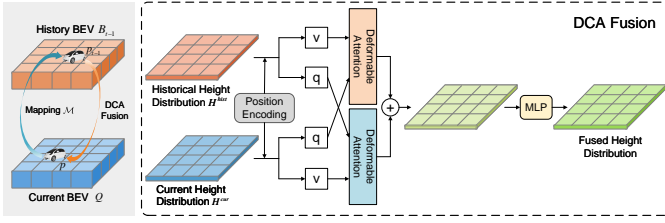


Fig. 3. The dual-branch cross-attention (DCA) fusion strategy between the current height distribution and historical height distribution. "q" represents the query, and "v" represents the value. In this figure, we omit the key because it corresponds to the center position  $p$  of the grid in the counterpart BEV space that is associated with the query, as determined by  $\mathcal{M}$ .

heights across the entire range, we propose an adaptive height-aware sampling method that enables the model to dynamically adjust the optimal sampling heights based on the specific scene characteristics.

Through TSA, each query  $Q_p$  looks up temporal information from its associated regions in history BEV  $B_{t-1}$ . To incorporate historical height information, we further generate a historical height distribution  $H_p^{hist} \in \mathbb{R}^{1 \times D}$  from  $B_{t-1}$ , where  $D$  denotes the number of discrete height bins over the global height range, by first establishing a mapping  $\mathcal{M}$  from time  $t$  to  $t-1$  enabling us to locate the previous position  $p_{t-1}$  of  $p$  prior to ego-motion. This mapping is defined as follows:

$$\mathcal{M} : p_{t-1} \leftarrow f_{t,t-1}^T (f_{t,t-1}^R (p, \mathbf{R}_{t,t-1}), \mathbf{T}_{t,t-1}), \quad (3)$$

where  $f_{t,t-1}^T$  and  $f_{t,t-1}^R$  denote the translation and rotation functions,  $\mathbf{T}_{t,t-1}$  and  $\mathbf{R}_{t,t-1}$  represent the translation vector and the rotation matrix of ego-motion from time  $t$  to  $t-1$  respectively. The relevant feature vector  $B_{t-1}^p$  associated with the grid region centering at  $p_{t-1}$  can be obtained to generate  $H_p^{hist}$  through the shared MLP and a softmax function, which are also utilized to estimate current height distribution  $H_p^{cur} \in \mathbb{R}^{1 \times D}$  of  $Q_p$ .

Following the above process, each query in  $Q$  produces both a current height distribution and a historical height distribution, which are then organized across the BEV space to form complete distributions for the entire BEV plane, represented as  $H^{cur}, H^{hist} \in \mathbb{R}^{H \times W \times D}$ . Unlike depth, the height of a moving object remains constant, allowing us to further refine the current height distribution prediction by merging  $H^{cur}$  and  $H^{hist}$ . Inspired by [26], we introduce a dual-branch cross-attention (DCA) fusion strategy to effectively integrate these height distributions. As shown in Fig.3, it consists of two deformable attention branches. In each branch, the height distribution  $H_p^{cur/hist}$  at each grid cell serves as the query, aggregating information related to the grid center position  $p$  from  $H^{hist/cur}$  in another branch:

$$\text{DCA}(H_p^{cur/hist}, H^{hist/cur}) = \text{DefAttn}(H_p^{cur/hist}, p, H^{hist/cur}). \quad (4)$$

The output distributions from both branches are then summed and passed through an MLP layer to generate the fused height distribution  $H^{fus} \in \mathbb{R}^{H \times W \times D}$ . For each resulting height distribution  $H_p^{fus}$ , we apply a top-K function to

sample  $N_{ref}$  discrete height values, which are subsequently used as the height coordinates of the 3D reference points in the horizontal cross-view feature aggregation.

#### D. Horizontal Cross-View Feature Aggregation

The standard spatial cross-attention (SCA) mechanism projects each 3D reference point to all image coordinate systems, summing features extracted from all hit views; this approach partially aggregates cross-view spatial information for 3D points that can be projected into adjacent views after coordinate transformation. However, for reference points projected into only one view, the imaging information of their associated objects may span multiple views, leading to inadequate feature aggregation. In this section, we present a graph-based horizontal cross-view feature aggregation (HCA) module, which learns a graph structure on the horizontal plane for each 3D reference point. As illustrated in Fig.4, this module refines each point's feature representation by integrating sampled features from neighboring nodes, thereby enhancing spatial correlations and improving global feature aggregation.

Formally, for any 3D reference point  $p_{3d} \in (x, y, z)$  in  $Q_p$ , where  $(x, y)$  represents the horizontal center coordinates of the corresponding grid region and  $z$  is the vertical height coordinate, we define a graph structure  $G = (\mathbf{A}, \mathbf{X}, \mathbf{V})$  centered on  $p_{3d}$ . Here,  $\mathbf{V} = \{v_k\}_{k=1}^M$  represents the set of nodes, where  $M$  denotes the number of  $p_{3d}$  and its neighbors, and  $v_1$  is the point  $p_{3d}$  itself; The adjacency matrix  $\mathbf{A} \in \mathbb{R}^{M \times M}$  is defined as a symmetric binary matrix representing an undirected graph, ensuring bidirectional connectivity between  $p_{3d}$  and its neighbors; And  $\mathbf{X} \in \mathbb{R}^{M \times C}$  represents the feature embeddings of all nodes, where the  $m$ -th feature vector  $\mathbf{x}_k \in \mathbb{R}^C$  corresponds to the attribute of  $v_k$ . Furthermore, each neighboring node  $v_k (k = 2, \dots, M)$  is learned from a linear layer:

$$v_k = p_{3d} + \Delta p_{xy} = (x + \Delta x, y + \Delta y, z), \quad (5)$$

$$\Delta p_{xy} = \text{Linear}(Q_p) \in \mathbb{R}^2, \quad (6)$$

where  $\Delta p_{xy} = (\Delta x, \Delta y)$  represent the sampling offsets along two dimensions of the horizontal plane. The feature vector of  $p_{3d}$ , denoted as  $\mathbf{x}_1$ , is obtained via deformable attention, similar to the vanilla SCA:

$$\mathbf{x}_1 = \frac{1}{|\mathcal{V}_{hit}|} \sum_{i \in \mathcal{V}_{hit}} \text{DefAttn}(Q_p, \mathcal{P}(p_{3d}, i), F_t^i), \quad (7)$$

where  $\mathcal{P}(p_{3d}, i)$  is the 2D point on  $i$ -th view projected from  $p_{3d}$  via the known intrinsic parameter matrix  $\mathbf{I}_i \in \mathbb{R}^{3 \times 4}$  of the  $i$ -th camera, which can be written as:

$$\mathcal{P}(p_{3d}, i) = (x_i, y_i), \quad (8)$$

$$z_i \cdot [x_i \ y_i \ 1]^T = \mathbf{I}_i \cdot [x \ y \ z \ 1]^T, \quad (9)$$

To optimize computational efficiency, the features of other neighboring nodes  $v_k (k = 2, \dots, M)$  are extracted from the corresponding image features using bilinear interpolation:

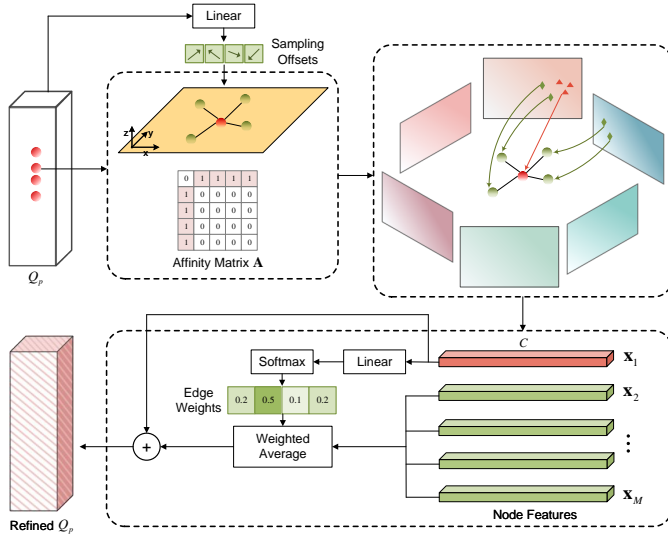


Fig. 4. The process of horizontal cross-view feature aggregation module. Each 3D reference point constructs a graph structure on its corresponding horizontal plane, where all neighboring nodes are projected onto the respective camera views using intrinsic parameters to extract features. These features are then aggregated through learned edge weights, effectively weighting the contributions of each neighboring node. This process enables the comprehensive aggregation of 3D spatial features for each query.

$$\mathbf{x}_k = \frac{1}{|\mathcal{V}_{hit}|} \sum_{i \in \mathcal{V}_{hit}} \text{Bilinear}(\mathcal{P}(v_k, i), F_t^i). \quad (10)$$

After obtaining the attributes of all nodes, we update the centered node features via:

$$\mathbf{x}'_1 = \mathbf{x}_1 + \sum_{k=2}^M \mathbf{A}_{1k} \cdot \mathbf{x}_k \cdot \mathbf{w}_{k-1}. \quad (11)$$

Here,  $\mathbf{w}$  represents the edge weight vector between  $p_{3d}$  and its neighbors, learned through a linear layer followed by a softmax function. Finally, the features of all  $N_{ref}$  reference points are aggregated via a weighted sum, yielding the refined query  $Q_p$  as the output of HCA module, fully enriched with spatial information.

### E. Overall Loss

Our training process follows the training phase of BEVFormer, sampling data from three historical timestamps within the previous two seconds to recursively generate historical BEV features  $B_{t-1}$  without gradient backpropagation. At the current time  $t$ , the model leverages both  $B_{t-1}$  and current multi-view images to capture temporal and spatial information, producing the BEV features  $B_t$ . These features are then passed to the detection head to predict 10 parameters for each 3D bounding box, including the center location, the scale of each box, the objects' yaw and velocity. The detector is trained end-to-end using ground-truth 3D bounding boxes. The loss used to supervise the training process includes classification loss  $L_{cls}$ , bounding box regression loss  $L_{reg}$ , and height distribution loss  $L_{hgt}$ :

$$L_{total} = \lambda_1 L_{cls} + \lambda_2 L_{reg} + \lambda_3 L_{hgt}, \quad (12)$$

where  $\lambda_1$ ,  $\lambda_2$  and  $\lambda_3$  are the balance weights assigned to the respective loss terms. We adopt focal loss [46] and L1 loss as the loss functions for classification and regression, respectively.  $L_{hgt}$  is a cross-entropy loss function defined to provide deep supervision for the estimated height distribution in the vertical adaptive height-aware sampling module. During training, we apply sparse supervision to  $H^{fus}$  through utilizing the height of the annotated 3D bounding box center.

Specifically, to facilitate the calculation of the discrepancy between the ground-truth height and the discretized predicted height distribution, we first derive the discretized ground-truth height distribution  $H_p^{gt}$  corresponding to each BEV grid region. Since an object's height is inherently a range rather than a fixed value, we employ a Gaussian kernel  $K$  to compute the differences between the annotated center height of an object and the predefined height bins. Height bins closer to the center are assigned higher probabilities. For convenience, we use an indicator  $I_p$  to denote whether the cell grid centered at  $p$  falls within the object's region. The probability corresponding to the  $m$ -th height bin of  $H_p^{gt}$  is calculated as:

$$H_{p,m}^{gt} = \begin{cases} \frac{K(z_{gt}, z_m)}{\sum_{n=1}^D K(z_{gt}, z_n)}, & I_p = 1 \\ 1/D, & I_p = 0 \end{cases}, \quad (10)$$

$$K(z_{gt}, z_m) = e^{-\frac{|z_{gt} - z_m|^2}{2\sigma^2}}, \quad (13)$$

where  $z_{gt}$  denotes the height of ground truth center,  $z_m$  represents the center value of the  $m$ -th height bin, and  $\sigma$  is the standard deviation controlling the spread of the Gaussian kernel. We then calculate the height distribution loss using cross-entropy as follows:

$$L_{hgt} = -\frac{1}{HW} \sum_{p \in \mathcal{P}_{bev}} H_p^{gt} \log H_p^{fus}. \quad (14)$$

Here, the grid set  $\mathcal{P}_{bev} = \{(i, j) | i = 1, \dots, H; j = 1, \dots, W\}$  is defined as the collection of all grid center positions on the BEV plane.

## IV. EXPERIMENTS

### A. Datasets and Metrics

**Dataset** We train and validate our model on the publicly available nuScenes [47] autonomous driving dataset. This dataset is constructed using six cameras providing a full 360° field of view, with images captured at a resolution of 1600×900 and a frequency of 12Hz. It also incorporates LiDAR sensors operating at 20Hz with a 360° horizontal field of view. The complete dataset consists of 1,000 diverse and challenging autonomous driving video sequences, collected from four distinct locations under varying weather and lighting conditions. Each sequence spans 20 seconds. Keyframes were sampled at a frequency of 2Hz for annotation, with 3D bounding boxes labeled for 10 object categories. Following the official dataset split, 28,130 frames from 750 sequences are used for training, while 6,019 and 6,008 frames from the

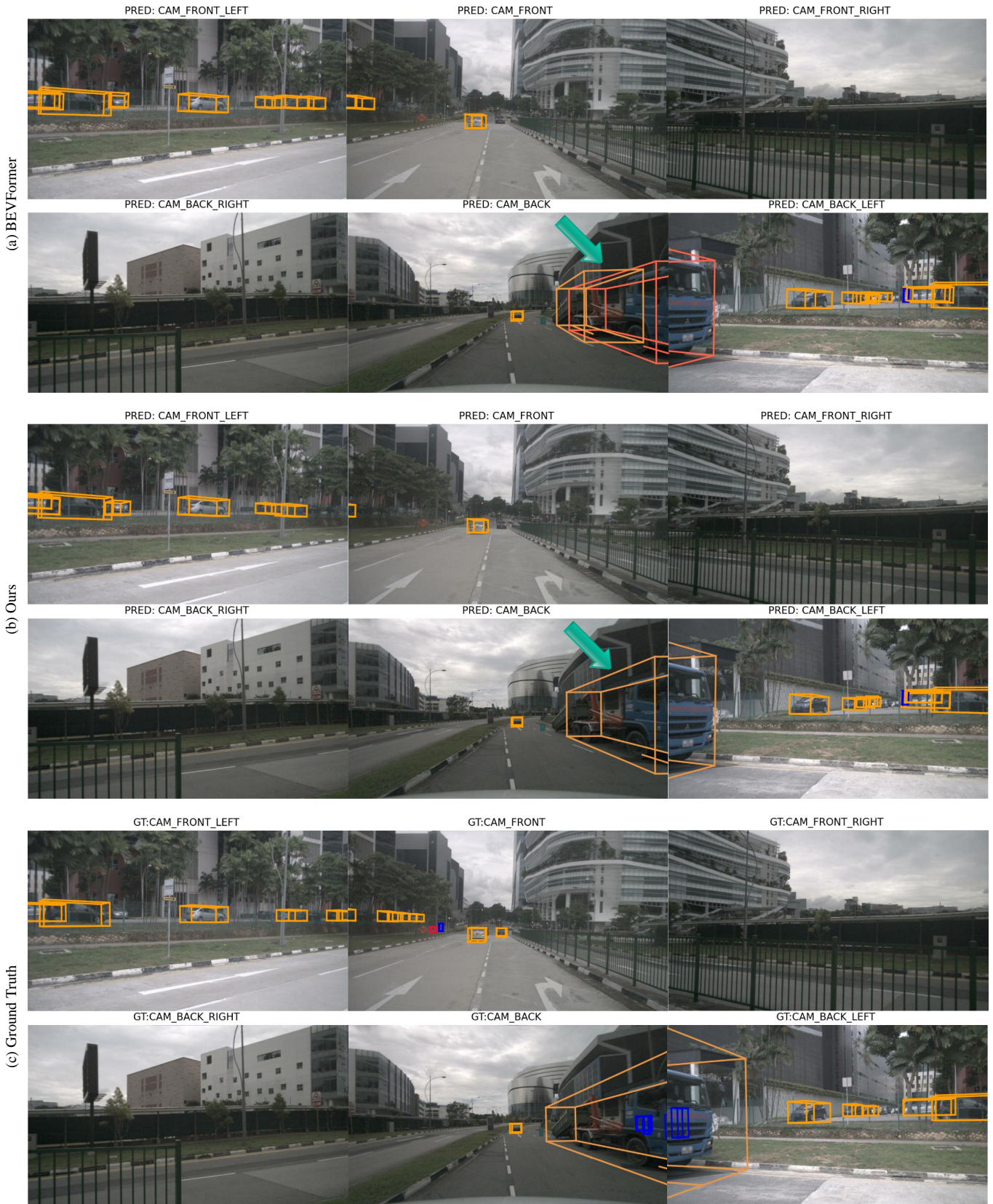


Fig. 5. Visualization results of HV-BEV and the baseline. The green arrows highlight instances where our method achieves improved detection performance on large cross-view objects. In BEVFormer, such objects are often missed or misdected due to view truncation. However, our approach enhances detection by leveraging a global focus on the structured characteristics of objects, effectively mitigating these challenges.

remaining 300 sequences are designated for validation and testing, respectively.

**Metrics** We evaluate the performance of our model using the 3D object detection metrics provided by the official nuScenes benchmark. These metrics include mean Average Precision (mAP), mean Average Translation Error (mATE), mean Average Scale Error (mASE), mean Average Orientation Error (mAOE), mean Average Velocity Error (mAVE), mean Average Attribute Error (mAAE), and the nuScenes Detection Score (NDS). Among these, mAP and NDS are the primary evaluation metrics.

### B. Implementation Details

Our model adopts BEVFormer as the baseline, with configurations tailored for two settings: *base* and *small*. Both settings share the same backbone, ResNet101-DCN [44], [48] and VoVnet-99 [54], initialized using pretrained parameters from FCOS3D [49] and DD3D [55], respectively. In the *base* setting, input images have a resolution of  $1600 \times 900$ , producing multi-scale features across four levels from the FPN, with a BEV grid size of  $200 \times 200$ , a historical sequence length of 4, and a BEV encoder comprising 6 layers. In contrast, the *small* setting uses input images of  $1280 \times 720$ , generates single-scale feature maps, and adopts a BEV grid size of  $150 \times 150$ , a historical sequence length of 3, and a BEV encoder with 3 layers. This design balances computational cost and performance while maintaining alignment with BEVFormer’s core architecture.

For the vertical adaptive height-aware module, the number of height bins is  $D = 8$ , and the number of 3D reference points sampled in each query is  $N_{ref} = 4$ . In the HCA module, each 3D reference point considers four neighboring nodes, and two sampling points are used for deformable attention when extracting features projected onto each 2D view. During training, the model uses the AdamW [50] optimizer with a cosine annealing learning rate schedule [51]. The initial learning rate is set to  $2 \times 10^{-4}$  and the weight decay is 0.01. Training is conducted on 8 NVIDIA L20 GPUs for 24 epochs.

### C. Main Results

**Performance Improvements Over Baseline** To comprehensively evaluate the performance improvements of our model, we configured it based on the three official configuration files provided by BEVFormer (i.e., tiny, small, and base) and trained it for the same number of epochs. The performance comparison on the nuScenes validation set is shown in Tab. I. Our model consistently outperforms the baseline in both key metrics, mAP and NDS, highlighting the effectiveness of our proposed optimization strategies. Under the *base* configuration, our model achieved improvements of 2.3% in mAP and 1.6% in NDS compared to the baseline. In Fig. 5, we visualize a comparison of 3D detection results between the proposed method and the baseline on a sample of nuScenes validation set. For large objects near the ego vehicle, our method demonstrates a significant improvement in detection accuracy. Fig. 6 illustrates the bird’s-eye view detection results for the same sample in the LIDAR point cloud. It can be

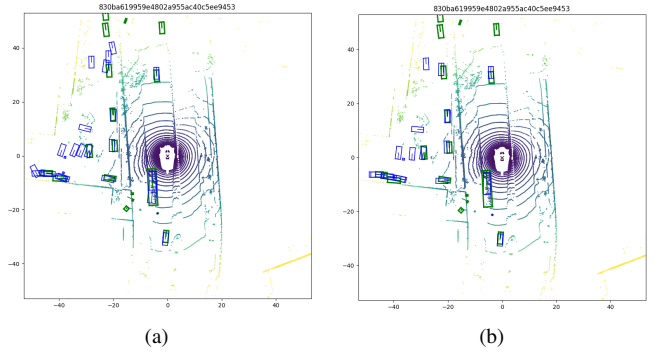


Fig. 6. Comparison of detection results in the LiDAR point cloud under the BEV perspective. (a) Baseline; (b) Ours. Green boxes represent ground truth annotations, while blue boxes denote predicted boxes.

TABLE I  
PERFORMANCE COMPARISON WITH THE BASELINE UNDER THREE DIFFERENT CONFIGURATIONS. FOR FAIRNESS, OUR MODEL STRICTLY FOLLOWS THE OFFICIAL CONFIGURATION FILES PROVIDED BY BEVFORMER.

| Model        | Config | Grid Size        | Backbone  | mAP $\uparrow$ | NDS $\uparrow$ |
|--------------|--------|------------------|-----------|----------------|----------------|
| BEVFormer    | tiny   | $50 \times 50$   | ResNet50  | 0.252          | 0.354          |
| HV-BEV(Ours) | tiny   | $50 \times 50$   | ResNet50  | <b>0.284</b>   | <b>0.378</b>   |
| BEVFormer    | small  | $150 \times 150$ | ResNet101 | 0.370          | 0.479          |
| HV-BEV(Ours) | small  | $150 \times 150$ | ResNet101 | <b>0.399</b>   | <b>0.502</b>   |
| BEVFormer    | base   | $200 \times 200$ | ResNet101 | 0.416          | 0.517          |
| HV-BEV(Ours) | base   | $200 \times 200$ | ResNet101 | <b>0.439</b>   | <b>0.533</b>   |

observed that our model exhibits fewer false positives and achieves a higher degree of overlap with the ground truth boxes. However, small distant objects remain challenging and are more prone to missed detections. Fig. 7 presents several robust detection results of HV-BEV for cross-view objects or large-scale objects. Our model demonstrates exceptional performance in handling such challenging scenarios.

**Comparison with State-of-the-Arts** In addition to comparing our model with the baseline, we also present a performance comparison between our approach and some other state-of-the-art 3D object detection methods on the nuScenes validation and testing sets. The results are summarized in Tab. II and Tab. III, respectively. On the validation set, we compared the performance of two model configurations. The *small* configuration achieved 39.9% mAP and 50.2 NDS, surpassing one of the latest methods, QAF2D [52], under similar settings. The *base* configuration achieved 43.9% mAP and 53.3% NDS, outperforming HeightFormer, which also incorporates explicit height information, under comparable configurations. On the testing set, we evaluated our method using two mainstream backbone networks. With VoVNet-99 as the backbone, our approach achieved 50.5% mAP and 59.8% NDS. Notably, our model demonstrated exceptional performance on the mAAE metric, likely due to its comprehensive consideration of spatial correlations of an object.

### D. Ablation Study

In order to gain deeper insights into the effectiveness of the proposed method’s individual components, we conducted

TABLE II  
3D DETECTION RESULTS ON nuSCENES *val* SET. “C” INDICATES CAMERA. \*: TRAINED WITH LIDAR DATA. †: PRE-TRAINED FROM FCOS3D. ‡: PRE-TRAINED FROM DD3D.

| Model                                   | Img Size   | Backbone  | mAP↑         | NDS↑         | mATE↓        | mASE↓        | mAOE↓        | mAVE↓        | mAAE↓        |
|---|------------|-----------|--------------|--------------|--------------|--------------|--------------|--------------|--------------|
| PETR† [21]                              | 1056 × 384 | ResNet101 | 0.347        | 0.423        | 0.736        | 0.269        | 0.448        | 0.844        | 0.202        |
| BEVFormer <sub>small</sub> -QAF2D† [52] | 1280 × 736 | ResNet101 | 0.397        | <b>0.502</b> | <b>0.703</b> | <b>0.274</b> | <b>0.369</b> | 0.404        | 0.213        |
| HV-BEV <sub>small</sub> †(Ours)         | 1280 × 720 | ResNet101 | <b>0.399</b> | <b>0.502</b> | 0.706        | 0.279        | 0.395        | <b>0.400</b> | <b>0.203</b> |
| DETR3D‡ [17]                            | 1600 × 900 | ResNet101 | 0.349        | 0.434        | 0.716        | 0.268        | 0.379        | 0.842        | 0.200        |
| BEVDet [13]                             | 1600 × 640 | Swin-T    | 0.393        | 0.472        | 0.608        | <b>0.259</b> | 0.366        | 0.822        | 0.191        |
| BEVDepth*‡ [15]                         | 1408 × 512 | ResNet101 | 0.418        | 0.538        | -            | -            | -            | -            | -            |
| GraphDETR3D‡ [23]                       | 1600 × 640 | ResNet101 | 0.369        | 0.447        | -            | -            | -            | -            | -            |
| PETRv2† [22]                            | 1600 × 640 | ResNet101 | 0.421        | 0.524        | 0.681        | 0.267        | 0.357        | 0.377        | 0.186        |
| OCBEV† [43]                             | 1600 × 900 | ResNet101 | 0.417        | 0.532        | 0.629        | 0.273        | 0.339        | 0.342        | 0.187        |
| Sparse4D <sub>T=4</sub> † [25]          | 1600 × 900 | ResNet101 | 0.436        | <b>0.541</b> | 0.633        | 0.279        | 0.363        | 0.317        | 0.177        |
| HeightFormer† [40]                      | 1600 × 900 | ResNet101 | 0.429        | 0.532        | -            | -            | -            | -            | -            |
| BEVDet4D+WidthFormer† [53]              | 1408 × 512 | ResNet101 | 0.423        | 0.531        | 0.609        | 0.269        | 0.412        | <b>0.302</b> | 0.210        |
| Fast-BEV† [12]                          | 1600 × 900 | ResNet101 | 0.413        | 0.535        | <b>0.584</b> | 0.279        | <b>0.311</b> | 0.329        | 0.206        |
| HV-BEV <sub>base</sub> †(Ours)          | 1600 × 900 | ResNet101 | <b>0.439</b> | 0.533        | 0.617        | 0.264        | 0.388        | 0.375        | <b>0.127</b> |

TABLE III  
3D DETECTION RESULTS ON nuSCENES *test* SET. “C” AND “L” INDICATES CAMERA AND LIDAR. \*: TRAINED WITH LIDAR DATA. †: PRE-TRAINED FROM FCOS3D. ‡: PRE-TRAINED FROM DD3D.

| Model                          | Modality | Img Size   | Backbone  | mAP↑         | NDS↑         | mATE↓        | mASE↓        | mAOE↓        | mAVE↓        | mAAE↓        |
|--------------------------------|----------|------------|-----------|--------------|--------------|--------------|--------------|--------------|--------------|--------------|
| CenterPoint [56]               | L        | -          | -         | 0.580        | 0.655        | -            | -            | -            | -            | -            |
| PointPainting [57]             | L+C      | -          | -         | 0.464        | 0.581        | 0.388        | 0.271        | 0.496        | 0.247        | 0.111        |
| BEVFusion [58]                 | L+C      | -          | -         | 0.717        | 0.738        | 0.252        | 0.238        | 0.321        | 0.265        | 0.126        |
| BEVDet4D [14]                  | C        | 1600 × 640 | Swin-T    | 0.451        | <b>0.569</b> | <b>0.511</b> | <b>0.241</b> | 0.386        | <b>0.301</b> | 0.121        |
| GraphDETR3D† [23]              | C        | 1600 × 640 | ResNet101 | 0.418        | 0.472        | 0.668        | 0.250        | 0.440        | 0.876        | 0.139        |
| PETRv2† [22]                   | C        | 1600 × 640 | ResNet101 | 0.456        | 0.553        | 0.601        | 0.249        | 0.391        | 0.382        | 0.123        |
| HV-BEV <sub>base</sub> †(Ours) | C        | 1600 × 900 | ResNet101 | <b>0.467</b> | 0.562        | 0.586        | 0.261        | <b>0.362</b> | 0.362        | <b>0.113</b> |
| DETR3D‡ [17]                   | C        | 1600 × 900 | VoVNet-99 | 0.412        | 0.479        | 0.641        | 0.255        | 0.394        | 0.845        | 0.133        |
| BEVDepth*‡ [15]                | C        | 1408 × 512 | VoVNet-99 | 0.503        | <b>0.600</b> | <b>0.445</b> | 0.245        | 0.378        | 0.320        | 0.126        |
| GraphDETR3D‡ [23]              | C        | 1600 × 640 | VoVNet-99 | 0.425        | 0.495        | 0.621        | 0.251        | 0.386        | 0.790        | 0.128        |
| PETRv2‡ [22]                   | C        | 1600 × 640 | VoVNet-99 | 0.490        | 0.582        | 0.561        | <b>0.243</b> | 0.361        | 0.343        | 0.120        |
| VEDet‡ [59]                    | C        | 1600 × 640 | VoVNet-99 | 0.505        | 0.585        | 0.545        | 0.244        | <b>0.346</b> | 0.421        | 0.123        |
| HeightFormer‡ [40]             | C        | 1600 × 900 | VoVNet-99 | 0.481        | 0.573        | -            | -            | -            | -            | -            |
| HV-BEV <sub>base</sub> ‡(Ours) | C        | 1600 × 900 | VoVNet-99 | <b>0.505</b> | 0.598        | 0.544        | 0.249        | 0.353        | <b>0.318</b> | <b>0.107</b> |

TABLE IV  
MAIN ABLATION RESULTS OF HV-BEV ON nuSCENES VAL SET. “VHA” AND “HCA” DENOTES FOR VERTICAL ADAPTIVE HEIGHT-AWARE SAMPLING AND HORIZONTAL CROSS-VIEW FEATURE AGGREGATION, RESPECTIVELY.

| VHA | HCA | mAP↑         | NDS↑         | mATE↓        | mASE↓        | mAOE↓        | mAVE↓        | mAAE↓        |
|-----|-----|--------------|--------------|--------------|--------------|--------------|--------------|--------------|
| ✗   | ✗   | 0.370        | 0.479        | 0.721        | 0.279        | 0.407        | 0.436        | 0.220        |
| ✓   | ✗   | 0.375        | 0.482        | 0.716        | 0.280        | 0.405        | 0.431        | 0.217        |
| ✗   | ✓   | 0.392        | 0.498        | 0.709        | <b>0.279</b> | 0.399        | 0.409        | 0.208        |
| ✓   | ✓   | <b>0.399</b> | <b>0.502</b> | <b>0.706</b> | <b>0.279</b> | <b>0.395</b> | <b>0.400</b> | <b>0.203</b> |

a series of ablation studies on the nuScenes validation set using the *small* configuration of our model.

**Main Ablations** In this subsection, we focus on validating the effectiveness of the proposed enhancement strategies. As shown in Tab. IV, the vanilla BEVFormer achieves an mAP of 37.0% and an NDS of 47.9%. Incorporating the Vertical Adaptive Height-Aware (VHA) sampling strategy improves these metrics by 0.5% and 0.3%, respectively. Adding the Horizontal Cross-view Feature Aggregation (HCA) module further boosts mAP and NDS by 2.2% and 1.9%, respectively. When both strategies are applied simultaneously, the mAP and NDS reach 39.9% and 50.2%, representing gains of 2.9% and 2.3%, respectively. Additionally, significant improvements are observed across other metrics as well.

**Ablations on VHA** In the VHA module, the number of height bins determines the sampling density of 3D reference points. Setting too few height bins (e.g., 4) degrade the model into uniform height sampling, similar to the vanilla BEVFormer. Conversely, an excessive number of height bins may cause reference points to overly concentrate within a narrow height range. Therefore, selecting an optimal number of height bins is crucial. Tab. V summarizes the experimental results for different height bin configurations. When the number of height bins is set to 8, the model achieves the best performance. The performance with 6 bins is only slightly lower than with 8 bins, but increasing the number of bins beyond 8 leads to a notable decline in performance. We infer that this decline occurs

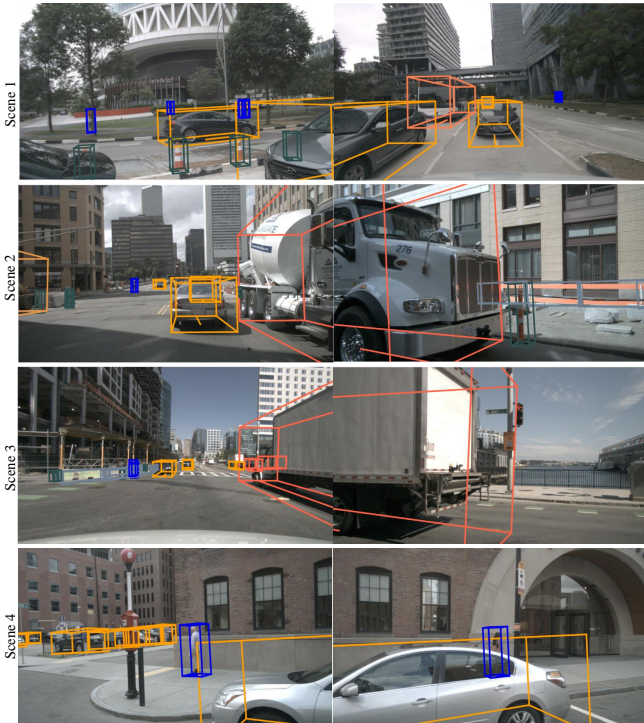


Fig. 7. Some robust detection results for cross-view objects and large-scale objects (such as trucks) on the nuScenes validation set. Different colors represent different object classes.

TABLE V  
EFFECTIVENESS OF THE NUMBER OF HEIGHT BINS IN VHA MODULE ON NUSCENES VAL SET.

| Height Bin Num | mAP $\uparrow$ | NDS $\uparrow$ | mATE $\downarrow$ | mAOE $\downarrow$ |
|----------------|----------------|----------------|-------------------|-------------------|
| 4              | 0.392          | 0.498          | 0.709             | 0.398             |
| 6              | 0.397          | 0.501          | <b>0.706</b>      | 0.396             |
| 8              | <b>0.399</b>   | <b>0.502</b>   | <b>0.706</b>      | <b>0.395</b>      |
| 10             | 0.381          | 0.486          | 0.719             | 0.411             |
| 12             | 0.372          | 0.476          | 0.760             | 0.419             |

because the supervision for the height distribution prediction is based on the 3D center of the object. As the number of bins increases and becomes denser, the 3D reference points are sampled closer to the object center, resulting in higher probabilities being assigned to bins near the center. This concentration on the central region may force the model to overlook the broader height range, thereby degrading overall performance.

**Ablations on HCA** In the HCA module, each 3D reference point constructs a horizontal dynamic graph centered on itself, with each node in the graph aggregating relevant features from its respective location. Theoretically, increasing the number of graph nodes allows the aggregation of richer features but also incurs higher computational costs. Determining the optimal number of neighboring nodes to balance accuracy and computational efficiency is a critical consideration. Tab. VI presents the model’s performance and memory usage under various settings for the number of neighbors. Interestingly, performance degrades when the number of neighbors becomes excessively large, potentially due to over-smoothing. We adopt

TABLE VI  
EFFECTIVENESS OF THE NUMBER OF NEIGHBORS IN HCA MODULE ON NUSCENES VAL SET.

| Neighbor Num | mAP $\uparrow$ | NDS $\uparrow$ | Memory        |
|--------------|----------------|----------------|---------------|
| 2            | 0.386          | 0.489          | $\sim$ 11700M |
| 4            | 0.399          | 0.502          | $\sim$ 13900M |
| 8            | 0.402          | 0.504          | $\sim$ 17150M |
| 16           | 0.379          | 0.480          | $\sim$ 22950M |

TABLE VII  
EFFECTIVENESS OF INCREASING THE NUMBER OF 3D REFERENCE POINTS WITHIN EACH QUERY ON NUSCENES VAL SET.

| Model        | Config | $N_{ref}$           | mAP $\uparrow$ | NDS $\uparrow$ |
|--------------|--------|---------------------|----------------|----------------|
| BEVFormer    | small  | 4                   | 0.370          | 0.479          |
|              |        | 8                   | 0.374          | 0.481          |
|              |        | 16                  | 0.351          | 0.462          |
| HV-BEV(Ours) | small  | 4 ( $\times$ 4 nbs) | <b>0.399</b>   | <b>0.502</b>   |

4 neighbors as the default configuration, which not only reduces memory usage but also maintains competitive accuracy.

**Effectiveness of decoupled sampling method** This study enhances feature aggregation through height-aware reference point sampling along the vertical axis and graph-based cross-view perception in the horizontal plane. However, it is generally acknowledged that increasing the number of reference points for a single query, without considering computational cost, inherently allows the sampling of more image features, thereby improving detection accuracy. The purpose of this section is to validate the effectiveness of the proposed feature sampling strategies, rather than attributing performance improvements solely to the increased number of reference points. Tab. VII reports the results of experiments conducted on the baseline model under the *small* configuration. These tests examine the effect of increasing the number of uniformly sampled 3D reference points per query ( $N_{ref} = 4, 8, 16$ ) on detection accuracy. The results indicate that increasing  $N_{ref}$  to 8 yields only minor performance improvements, while further increasing it to 16 results in a decline across all metrics. We attribute this decline to the potential redundancy or irrelevance introduced by simply adding more uniformly sampled reference points, which may weaken the impact of critical features and disrupt the model’s learning process. These findings further validate the effectiveness of the proposed decoupled horizontal and vertical feature sampling strategies.

## V. CONCLUSION

In this paper, we propose HV-BEV, a novel dense BEV-based 3D object detection framework that decouples horizontal and vertical feature sampling. The framework leverages adaptive height-aware 3D reference point sampling by integrating historical and current BEV height distributions to focus on object-relevant height ranges. It then learns a graph structure on the horizontal plane at the reference points’ corresponding heights, enabling the aggregation of structured spatial information for objects in 3D space. Finally, we introduce a loss function with depth supervision, utilizing the ground-truth center height of objects to refine the predicted height

distribution. Extensive experiments on the nuScenes dataset validate the effectiveness of the proposed approach.

Our approach aims to serve as a reference for dense BEV-based 3D perception tasks beyond object detection. However, while our method significantly improves detection accuracy, it shares a limitation with the baseline model (i.e., BEVFormer): high computational cost. In future work, we plan to explore hybrid perception models that combine dense and sparse BEV representations to further optimize model performance while reducing computational overhead.

## REFERENCES

- [1] J. Mao, S. Shi, X. Wang, and H. Li, “3d object detection for autonomous driving: A comprehensive survey,” *International Journal of Computer Vision*, vol. 131, no. 8, pp. 1909–1963, 2023.
- [2] C. R. Qi, H. Su, K. Mo, and L. J. Guibas, “Pointnet: Deep learning on point sets for 3d classification and segmentation,” in *Proceedings of the IEEE conference on computer vision and pattern recognition*, 2017, pp. 652–660.
- [3] C. R. Qi, L. Yi, H. Su, and L. J. Guibas, “Pointnet++: Deep hierarchical feature learning on point sets in a metric space,” *Advances in neural information processing systems*, vol. 30, 2017.
- [4] Y. Zhou and O. Tuzel, “Voxelnet: End-to-end learning for point cloud based 3d object detection,” in *Proceedings of the IEEE conference on computer vision and pattern recognition*, 2018, pp. 4490–4499.
- [5] Z. Liu, X. Ye, Z. Zou, X. He, X. Tan, E. Ding, J. Wang, and X. Bai, “Multi-modal 3d object detection by box matching,” *IEEE Transactions on Intelligent Transportation Systems*, 2024.
- [6] J. Li, Z. Wang, D. Gong, and C. Wang, “Scnet3d: Rethinking the feature extraction process of pillar-based 3d object detection,” *IEEE Transactions on Intelligent Transportation Systems*, 2024.
- [7] A. Singh, “Surround-view vision-based 3d detection for autonomous driving: A survey,” in *2023 IEEE/CVF International Conference on Computer Vision Workshops (ICCVW)*. IEEE, 2023, pp. 3235–3244.
- [8] Y. Ma, T. Wang, X. Bai, H. Yang, Y. Hou, Y. Wang, Y. Qiao, R. Yang, and X. Zhu, “Vision-centric bev perception: A survey,” *IEEE Transactions on Pattern Analysis and Machine Intelligence*, 2024.
- [9] Y. Zhang, Z. Zhu, and D. Du, “Occformer: Dual-path transformer for vision-based 3d semantic occupancy prediction,” in *Proceedings of the IEEE/CVF International Conference on Computer Vision*, 2023, pp. 9433–9443.
- [10] Y. Huang, W. Zheng, Y. Zhang, J. Zhou, and J. Lu, “Gaussianformer: Scene as gaussians for vision-based 3d semantic occupancy prediction,” *arXiv preprint arXiv:2405.17429*, 2024.
- [11] E. Xie, Z. Yu, D. Zhou, J. Philion, A. Anandkumar, S. Fidler, P. Luo, and J. M. Alvarez, “M<sup>2</sup>bev: Multi-camera joint 3d detection and segmentation with unified birds-eye view representation,” *arXiv preprint arXiv:2204.05088*, 2022.
- [12] Y. Li, B. Huang, Z. Chen, Y. Cui, F. Liang, M. Shen, F. Liu, E. Xie, L. Sheng, W. Ouyang *et al.*, “Fast-bev: A fast and strong bird’s-eye view perception baseline,” *IEEE Transactions on Pattern Analysis and Machine Intelligence*, 2024.
- [13] J. Huang, G. Huang, Z. Zhu, Y. Ye, and D. Du, “Bevdet: High-performance multi-camera 3d object detection in bird-eye-view,” *arXiv preprint arXiv:2112.11790*, 2021.
- [14] J. Huang and G. Huang, “Bevdet4d: Exploit temporal cues in multi-camera 3d object detection,” *arXiv preprint arXiv:2203.17054*, 2022.
- [15] Y. Li, Z. Ge, G. Yu, J. Yang, Z. Wang, Y. Shi, J. Sun, and Z. Li, “Bevdepth: Acquisition of reliable depth for multi-view 3d object detection,” in *Proceedings of the AAAI Conference on Artificial Intelligence*, vol. 37, no. 2, 2023, pp. 1477–1485.
- [16] Y. Li, H. Bao, Z. Ge, J. Yang, J. Sun, and Z. Li, “Bevstereo: Enhancing depth estimation in multi-view 3d object detection with temporal stereo,” in *Proceedings of the AAAI Conference on Artificial Intelligence*, vol. 37, no. 2, 2023, pp. 1486–1494.
- [17] Y. Wang, V. C. Guizilini, T. Zhang, Y. Wang, H. Zhao, and J. Solomon, “Detr3d: 3d object detection from multi-view images via 3d-to-2d queries,” in *Conference on Robot Learning*. PMLR, 2022, pp. 180–191.
- [18] Z. Li, W. Wang, H. Li, E. Xie, C. Sima, T. Lu, Y. Qiao, and J. Dai, “Bevformer: Learning bird’s-eye-view representation from multi-camera images via spatiotemporal transformers,” in *European conference on computer vision*. Springer, 2022, pp. 1–18.
- [19] C. Yang, Y. Chen, H. Tian, C. Tao, X. Zhu, Z. Zhang, G. Huang, H. Li, Y. Qiao, L. Lu *et al.*, “Bevformer v2: Adapting modern image backbones to bird’s-eye-view recognition via perspective supervision,” in *Proceedings of the IEEE/CVF Conference on Computer Vision and Pattern Recognition*, 2023, pp. 17830–17839.
- [20] X. Zhu, W. Su, L. Lu, B. Li, X. Wang, and J. Dai, “Deformable detr: Deformable transformers for end-to-end object detection,” in *International Conference on Learning Representations*, 2021.
- [21] Y. Liu, T. Wang, X. Zhang, and J. Sun, “Petr: Position embedding transformation for multi-view 3d object detection,” in *European Conference on Computer Vision*. Springer, 2022, pp. 531–548.
- [22] Y. Liu, J. Yan, F. Jia, S. Li, A. Gao, T. Wang, and X. Zhang, “Petrv2: A unified framework for 3d perception from multi-camera images,” in *Proceedings of the IEEE/CVF International Conference on Computer Vision*, 2023, pp. 3262–3272.
- [23] Z. Chen, Z. Li, S. Zhang, L. Fang, Q. Jiang, and F. Zhao, “Graph-detr3d: rethinking overlapping regions for multi-view 3d object detection,” in *Proceedings of the 30th ACM International Conference on Multimedia*, 2022, pp. 5999–6008.
- [24] Z. Chen, Z. Chen, Z. Li, S. Zhang, L. Fang, Q. Jiang, F. Wu, and F. Zhao, “Graph-detr4d: Spatio-temporal graph modeling for multi-view 3d object detection,” *IEEE Transactions on Image Processing*, 2024.
- [25] X. Lin, T. Lin, Z. Pei, L. Huang, and Z. Su, “Sparse4d: Multi-view 3d object detection with sparse spatial-temporal fusion,” *arXiv preprint arXiv:2211.10581*, 2022.
- [26] X. Chi, J. Liu, M. Lu, R. Zhang, Z. Wang, Y. Guo, and S. Zhang, “Bev-san: Accurate bev 3d object detection via slice attention networks,” in *Proceedings of the IEEE/CVF Conference on Computer Vision and Pattern Recognition*, 2023, pp. 17461–17470.
- [27] J. Philion and S. Fidler, “Lift, splat, shoot: Encoding images from arbitrary camera rigs by implicitly unprojecting to 3d,” in *Computer Vision—ECCV 2020: 16th European Conference, Glasgow, UK, August 23–28, 2020, Proceedings, Part XIV 16*. Springer, 2020, pp. 194–210.
- [28] C. Reading, A. Harakeh, J. Chae, and S. L. Waslander, “Categorical depth distribution network for monocular 3d object detection,” in *Proceedings of the IEEE/CVF Conference on Computer Vision and Pattern Recognition*, 2021, pp. 8555–8564.
- [29] J. Park, C. Xu, S. Yang, K. Keutzer, K. Kitani, M. Tomizuka, and W. Zhan, “Time will tell: New outlooks and a baseline for temporal multi-view 3d object detection,” *arXiv preprint arXiv:2210.02443*, 2022.
- [30] Z. Li, Z. Yu, W. Wang, A. Anandkumar, T. Lu, and J. M. Alvarez, “Fb-bev: Bev representation from forward-backward view transformations,” in *Proceedings of the IEEE/CVF International Conference on Computer Vision*, 2023, pp. 6919–6928.
- [31] Z. Li, S. Lan, J. M. Alvarez, and Z. Wu, “Bevnext: Reviving dense bev frameworks for 3d object detection,” in *Proceedings of the IEEE/CVF Conference on Computer Vision and Pattern Recognition*, 2024, pp. 20113–20123.
- [32] C. Han, J. Yang, J. Sun, Z. Ge, R. Dong, H. Zhou, W. Mao, Y. Peng, and X. Zhang, “Exploring recurrent long-term temporal fusion for multi-view 3d perception,” *IEEE Robotics and Automation Letters*, 2024.
- [33] X. Lin, T. Lin, Z. Pei, L. Huang, and Z. Su, “Sparse4d v2: Recurrent temporal fusion with sparse model,” *arXiv preprint arXiv:2305.14018*, 2023.
- [34] A. Vaswani, “Attention is all you need,” *Advances in Neural Information Processing Systems*, 2017.
- [35] T. B. Brown, “Language models are few-shot learners,” *arXiv preprint arXiv:2005.14165*, 2020.
- [36] Z. Liu, Y. Lin, Y. Cao, H. Hu, Y. Wei, Z. Zhang, S. Lin, and B. Guo, “Swin transformer: Hierarchical vision transformer using shifted windows,” in *Proceedings of the IEEE/CVF international conference on computer vision*, 2021, pp. 10012–10022.
- [37] A. Dosovitskiy, L. Beyer, A. Kolesnikov, D. Weissenborn, X. Zhai, T. Unterthiner, M. Dehghani, M. Minderer, G. Heigold, and S. Gelly, “An image is worth 16x16 words: Transformers for image recognition at scale,” in *International Conference on Learning Representations*, 2021.
- [38] N. Carion, F. Massa, G. Synnaeve, N. Ununier, A. Kirillov, and S. Zagoruyko, “End-to-end object detection with transformers,” in *European conference on computer vision*. Springer, 2020, pp. 213–229.
- [39] Y. Zhao, W. Lv, S. Xu, J. Wei, G. Wang, Q. Dang, Y. Liu, and J. Chen, “Detrs beat yolos on real-time object detection,” in *Proceedings of the IEEE/CVF Conference on Computer Vision and Pattern Recognition*, 2024, pp. 16965–16974.
- [40] Y. Wu, R. Li, Z. Qin, X. Zhao, and X. Li, “Heightformer: Explicit height modeling without extra data for camera-only 3d object detection in bird’s eye view,” *IEEE Transactions on Image Processing*, 2024.

- [41] L. Yang, K. Yu, T. Tang, J. Li, K. Yuan, L. Wang, X. Zhang, and P. Chen, "Bevheight: A robust framework for vision-based roadside 3d object detection," in *Proceedings of the IEEE/CVF Conference on Computer Vision and Pattern Recognition*, 2023, pp. 21 611–21 620.
- [42] L. Yang, T. Tang, J. Li, P. Chen, K. Yuan, L. Wang, Y. Huang, X. Zhang, and K. Yu, "Bevheight++: Toward robust visual centric 3d object detection," *arXiv preprint arXiv:2309.16179*, 2023.
- [43] Z. Qi, J. Wang, X. Wu, and H. Zhao, "Ocbev: Object-centric bev transformer for multi-view 3d object detection," in *2024 International Conference on 3D Vision (3DV)*. IEEE, 2024, pp. 1188–1197.
- [44] K. He, X. Zhang, S. Ren, and J. Sun, "Deep residual learning for image recognition," in *Proceedings of the IEEE conference on computer vision and pattern recognition*, 2016, pp. 770–778.
- [45] T.-Y. Lin, P. Dollár, R. Girshick, K. He, B. Hariharan, and S. Belongie, "Feature pyramid networks for object detection," in *Proceedings of the IEEE conference on computer vision and pattern recognition*, 2017, pp. 2117–2125.
- [46] T.-Y. Ross and G. Dollár, "Focal loss for dense object detection," in *proceedings of the IEEE conference on computer vision and pattern recognition*, 2017, pp. 2980–2988.
- [47] H. Caesar, V. Bankiti, A. H. Lang, S. Vora, V. E. Liong, Q. Xu, A. Krishnan, Y. Pan, G. Baldan, and O. Beijbom, "nusenes: A multimodal dataset for autonomous driving," in *Proceedings of the IEEE/CVF conference on computer vision and pattern recognition*, 2020, pp. 11 621–11 631.
- [48] J. Dai, H. Qi, Y. Xiong, Y. Li, G. Zhang, H. Hu, and Y. Wei, "Deformable convolutional networks," in *Proceedings of the IEEE international conference on computer vision*, 2017, pp. 764–773.
- [49] T. Wang, X. Zhu, J. Pang, and D. Lin, "Fcos3d: Fully convolutional one-stage monocular 3d object detection," in *Proceedings of the IEEE/CVF International Conference on Computer Vision*, 2021, pp. 913–922.
- [50] I. Loshchilov, "Decoupled weight decay regularization," *arXiv preprint arXiv:1711.05101*, 2017.
- [51] I. Loshchilov and F. Hutter, "Sgdr: Stochastic gradient descent with warm restarts," *arXiv preprint arXiv:1608.03983*, 2016.
- [52] H. Ji, P. Liang, and E. Cheng, "Enhancing 3d object detection with 2d detection-guided query anchors," in *Proceedings of the IEEE/CVF Conference on Computer Vision and Pattern Recognition*, 2024, pp. 21 178–21 187.
- [53] C. Yang, T. Lin, L. Huang, and E. J. Crowley, "Widthformer: Toward efficient transformer-based bev view transformation," *arXiv preprint arXiv:2401.03836*, 2024.
- [54] Y. Lee, J.-w. Hwang, S. Lee, Y. Bae, and J. Park, "An energy and gpu-computation efficient backbone network for real-time object detection," in *Proceedings of the IEEE/CVF conference on computer vision and pattern recognition workshops*, 2019, pp. 0–0.
- [55] D. Park, R. Ambrus, V. Guizilini, J. Li, and A. Gaidon, "Is pseudo-lidar needed for monocular 3d object detection?" in *Proceedings of the IEEE/CVF International Conference on Computer Vision*, 2021, pp. 3142–3152.
- [56] T. Yin, X. Zhou, and P. Krahenbuhl, "Center-based 3d object detection and tracking," in *Proceedings of the IEEE/CVF conference on computer vision and pattern recognition*, 2021, pp. 11 784–11 793.
- [57] S. Vora, A. H. Lang, B. Helou, and O. Beijbom, "Pointpainting: Sequential fusion for 3d object detection," in *Proceedings of the IEEE/CVF conference on computer vision and pattern recognition*, 2020, pp. 4604–4612.
- [58] Z. Liu, H. Tang, A. Amini, X. Yang, H. Mao, D. L. Rus, and S. Han, "Bevfusion: Multi-task multi-sensor fusion with unified bird's-eye view representation," in *2023 IEEE international conference on robotics and automation (ICRA)*. IEEE, 2023, pp. 2774–2781.
- [59] D. Chen, J. Li, V. Guizilini, R. A. Ambrus, and A. Gaidon, "Viewpoint equivariance for multi-view 3d object detection," in *Proceedings of the IEEE/CVF Conference on Computer Vision and Pattern Recognition*, 2023, pp. 9213–9222.